THE JOURNAL OF PHYSICAL CHEMISTRY LETTERS
A JOURNAL OF THE AMERICAN CHEMICAL SOCIETY

pubs.acs.org/JPCL

Letter

Direct Measurement of Charge Transfer Probability during Photodissociation of Few-keV OD^+ Beam

Chandan Bagdia, T. Severt, Naoki Iwamoto, Anjali Filinovich, T. N. Rescigno, A. E. Orel, K. D. Carnes, and I. Ben-Itzhak*

Cite This: *J. Phys. Chem. Lett.* 2024, 15, 6859−6865

Read Online

ACCESS | Metrics & More | Article Recommendations | Supporting Information

ABSTRACT: We have measured the photodissociation of few-keV OD^+ molecular ions into either $D^+ + O$ or $O^+ + D$ final products. The three-dimensional momentum imaging measurements of the light and massive fragments in coincidence were enabled by using an upgraded two-detector setup. In this work, we show that absorption of a single 790 or 395 nm photon excites the OD^+ from its electronic ground state to the B $^3\Sigma^-$ state, which dissociates to the $O^+(^4S) + D$ dissociation limit. To reach the other nearly degenerate dissociation limit, $D^+ + O(^3P)$, a unimolecular charge transfer, B $^3\Sigma^-$ to X $^3\Sigma^-$, transition is required following the same photoexcitation. The measured branching ratio of these dissociation channels is a direct measure of the charge transfer transition probability. This measured probability as a function of energy above the dissociation limit agrees well with our calculations.

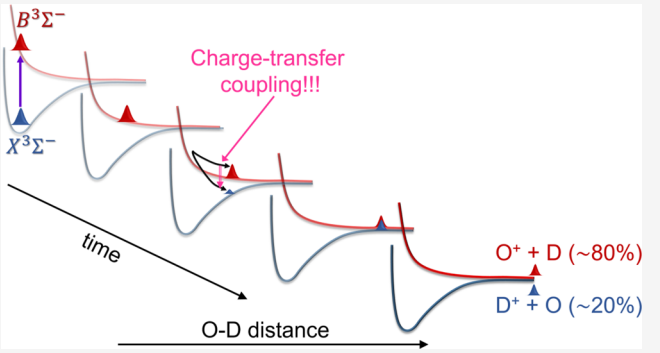

Early studies of OH^+ dissociation into $O^+ + H$ employing photofragment spectroscopy[1] have been motivated by the important role of the charge-exchange reaction, $H^+ + O \rightarrow O^+ + H$, which is the first step in the chemical cycle leading to OH formation in interstellar clouds.[2] Specifically, Helm et al.[1] experimentally explored the X $^3\Sigma^- \rightarrow$ A $^3\Pi$ transitions and the unimolecular mechanisms leading to the $O^+ + H$ dissociation limit.

More recently, Hechtfischer et al.[3] conducted a high-resolution study of the same X $^3\Sigma^- \rightarrow$ A $^3\Pi$ transitions just above the lowest OH^+ dissociation threshold, which is linked to the nearly degenerate $H^+ + O(^3P)$ and $O^+(^4S) + H$ dissociation limits. The detailed information they reported[3] can guide theoretical treatment of the $H^+ + O \rightarrow O^+ + H$ charge exchange reactions, which are key in the conversion of population in the excited A $^3\Pi$ state, associated with the $H^+ + O$ limit, to the $O^+ + H$ final products.

An OH^+ molecular ion beam also has population in its metastable states, specifically the electronic a $^1\Delta$ and b $^1\Sigma^+$ singlet states, and those can also contribute to the $H^+ + O$ and $O^+ + H$ dissociation channels. The role of these states in OH^+ dissociation was studied by Rodgers et al.,[4,5] who specifically explored their excitation to the predissociating c $^1\Pi$ state. The dissociation of the c $^1\Pi$ state of OH^+ was also measured by Levick et al.,[6] who showed that the *e*/*f* symmetry affects the branching ratio of the two dissociation channels. The predissociation of this c $^1\Pi$ state was later treated theoretically by Yarkony.[7]

Returning to the OH^+ triplet states of interest in this work, it has been found by Spirko et al.[8,9] that the coupling between the X $^3\Sigma^-$ and A $^3\Pi$ states dominates the calculated charge-exchange cross sections at low collision energy. These quantum mechanical calculations, however, describe the full collision, while in dissociation the internuclear distance starts from the "closest approach" and extends to infinity and thus is viewed as a "half collision". The important aspect of a "half collision" is that it allows one to associate the measured branching ratio between the two final channels directly with the calculated square of the transition amplitude between the two states. Such a half-collision approach was used, for example, by Wells et al.[10,11] to compare theory and experiment in the fundamental $H^+ + D(1s) \rightarrow D^+ + H(1s)$ charge-transfer reaction as a function of collision energy down to threshold (we use charge transfer in half collisions to distinguish them from charge exchange in full collisions).

In this work, we photoexcite a beam of OD^+ molecular ions from their electronic ground state, X $^3\Sigma^-$, to the B $^3\Sigma^-$ state that dissociates to the $O^+(^4S) + D$ limit (as detailed below,

Received: February 28, 2024
Revised: June 16, 2024
Accepted: June 17, 2024
Published: June 26, 2024

https://doi.org/10.1021/acs.jpclett.4c00649
J. Phys. Chem. Lett. 2024, 15, 6859−6865

OD^+ is studied instead of OH^+ for technical reasons). If a charge-transfer transition, from the B $^3\Sigma^-$ to the X $^3\Sigma^-$ state, occurs during stretching of the O−D bond, then the $D^+ + O(^3P)$ dissociation limit can be reached. The branching ratio of the $D^+ + O$ and $O^+ + D$ dissociation channels is a direct measure of the charge-transfer transition probability. We show below that the measured branching ratio as a function of energy above the dissociation limit, spanned by photoexcitation from different vibrational levels of the X state, agrees well with our *ab initio* calculations of this transition probability driven by radial coupling between the B and X states. All of the theoretical calculations were carried out using the MESA suite of quantum chemistry codes.[12]

The potential energy curves of the OD^+ molecular ion are shown in Figure 1. They were obtained from multireference

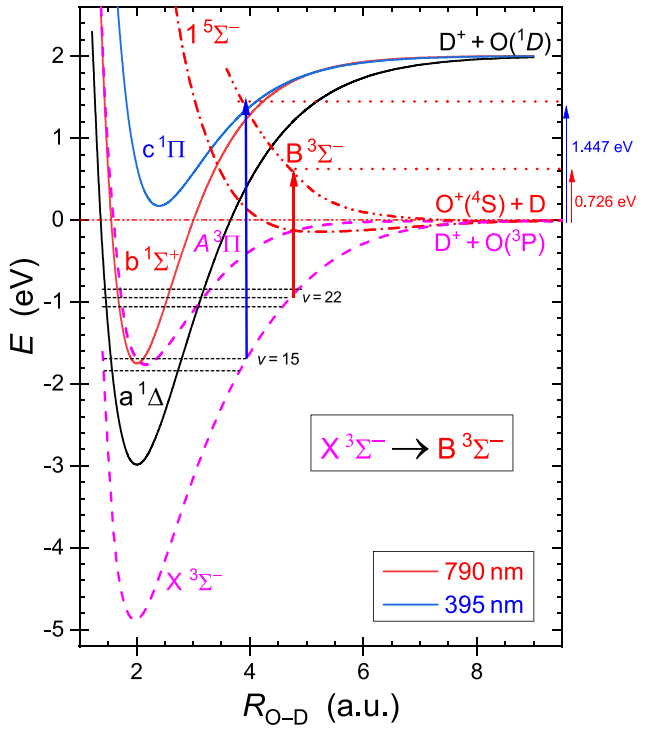

Figure 1. Potential energy curves of OD^+, where solid lines are the singlet states linked to the $D^+ + O(^1D)$ dissociation limit, dashed lines are triplet states associated with the $D^+ + O(^3P)$ limit, and dash-dot-dot and dash-dot lines are triplet and quintet states, respectively, dissociating to $O^+(^4S) + D(1s)$. The photoexcitation from the ground electronic state, X $^3\Sigma^-$, to the B $^3\Sigma^-$ state is marked by red (790 nm) and blue (395 nm) arrows as are their expected KER values.

single- and double-excitation configuration-interaction (MRCI) calculations using a basis of molecular orbitals obtained from multiconfiguration self-consistent field (MCSCF) calculations on the X $^3\Sigma^-$ ground state of OD^+. The Gaussian basis employed was the Dunning−Huzinaga triple-ζ plus polarization basis, augmented with one s-type, one p-type, and three d-type functions on oxygen, and the active space for the MCSCF calculations contained eight orbitals, with the O(1s) orbital held doubly occupied. Our calculations are entirely consistent with earlier theoretical calculations,[7,13−15] and as with previous *ab initio* calculations, the asymptotes of the states that dissociate to $O(^3P) + D^+$ are incorrectly placed above those that dissociate to $O^+(^4S) + D$, when in fact they are nearly degenerate. This error stems from the difficulty of calculating the relative ionization potentials (IPs) of atomic oxygen (which is challenging) and atomic hydrogen (which is easy). In the present context, in which the dissociation mechanism involves transitions at large O−D separations, we compensate for the asymptotic error by shifting the relevant $O^+ + D$ curves upward to ensure the proper asymptotic splitting.

There are three groups of states linked to different dissociation limits: (i) the X $^3\Sigma^-$ and A $^3\Pi$ (dashed magenta lines) are associated with the $D^+ + O(^3P)$ dissociation limit, (ii) the B $^3\Sigma^-$ and 1 $^5\Sigma^-$ (dash-dot-dot and dash-dot, red lines, respectively) are associated with the $O^+(^4S) + D$ dissociation limit, and (iii) the a $^1\Delta$, b $^1\Sigma^+$, and c $^1\Pi$ singlet states (solid black, red, and blue lines, respectively) are associated with the $D^+ + O(^1D)$ dissociation limit.

In Figure 1, we also indicate the photoexcitation scheme employed in the experiment and the expected kinetic energy release (KER) associated with the photodissociation of the $v = 22$ vibrational level by 790 nm photons and $v = 15$ by 395 nm photons. A few vibrational levels around $v = 15$ and 22, shown in Figure 1, were calculated using the phase-amplitude method.[17]

To conduct this photodissociation experiment we produced 395 nm photons by second harmonic generation of the 790 nm fundamental beam, provided by our 10 kHz laser known as PULSAR, in a type I beta-barium borate (BBO) crystal. Specifically, the 790 nm laser pulses used in the experiment were ∼28 fs wide (FWHM in intensity) with a peak intensity of 7.4×10^{13} W/cm^2. The 395 nm pulses were somewhat longer ∼40 fs (FWHM) and more intense, 3.8×10^{14} W/cm^2.

The 395 nm (790 nm) laser beam is then crossed with the OD^+ ion beam, and the resulting fragments of the interaction are measured downstream as described briefly below. The laser polarization is linear and aligned along the spectrometer axis.

The OD^+ ions were produced from D_2O vapor in an electron cyclotron resonance (ECR) ion source, accelerated to 25 keV, and selected using a magnet. The beam was then directed, after proper focusing and collimation, through the interaction region of the setup shown in Figure 2 and finally deflected into a small (4 mm diameter) Faraday cup, which is used to monitor the beam current (∼1 nA; see the Supporting

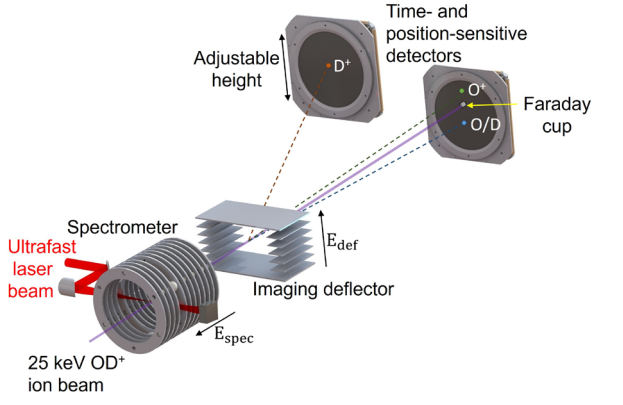

Figure 2. Schematic of the two-detector imaging setup used for the OD^+ dissociation measurements. Note that the detector used for the D^+ fragments, which was the key upgrade addition, can be translated along the vertical axis and is about halfway to the other detector.[16]

https://doi.org/10.1021/acs.jpclett.4c00649
J. Phys. Chem. Lett. 2024, 15, 6859−6865

Information), for normalization of the measurements to each other and to protect the imaging detector. The deflection of the ion beam between the interaction region and the Faraday cup enables the measurement of fragments with low KER, which otherwise would be "lost" in the Faraday cup.[18,19]

The deuterated OD^+, used in the present experiment, is expected to yield similar results as an OH^+, as both have similar electronic structure. However, the OD^+ has some technical advantages due to its smaller mass ratio, namely, a smaller image size of the light fragments, D^+ and D, and a higher detection efficiency than the respective H^+ and H fragments of OH^+.

To improve the ability to detect the light D and D^+ fragments in coincidence with the more massive O and O^+, we implemented a two detector imaging scheme[16] in which one detector is dedicated to the detection of the D^+ fragments while the other detects the rest of the fragments, as shown in Figure 2. We introduce, in this paper, the upgraded beam fragment momentum imaging setup, which was limited to a mass ratio of about 6−7 before,[20,21] and provide a few key details about the modifications. Measurements with a mass ratio of 14 were already conducted (and ∼20 within reach).

The detector placed on the ion-beam axis, an 80 mm diameter microchannel-plate (MCP) detector with a hex-delay line anode,[22] has been used in our previous studies.[19,23] About halfway to that detector we installed a similar detector that can be translated vertically, i.e., parallel to the electric field of the imaging detector. This detector has a larger MCP diameter of 120 mm to enable the detection of light fragments, such as protons (or deuterons), which typically have a large spread on the detector plane. The shorter distance from the interaction region to this detector also helps confine the light fragments within the detector. Here, too, the position information is decoded using a delay-line anode; however, a smaller and lighter anode with only two wires was used to facilitate the detector translation. The system electronics have been duplicated to allow recording the signals from both detectors for each laser pulse (further details of this setup can be found in Severt's PhD thesis[16]).

As stated above, the fragments of OD^+, both charged and neutral, are measured by a time- and position-sensitive detector.[22] The time and position signals are recorded event by event relative to a time signal produced by scattering some of the laser light onto a photodiode. This measured time and position information from both detectors is used to determine the momenta of both fragments in the moving center-of-mass frame of the OD^+, utilizing an upgraded code that includes the added detector.[16] Then, using these momenta, we evaluate the angular and KER distributions.

One should note that all the fragment trajectories in this experiment are within the 4π collection angles of the detectors. However, some of the fragments are lost, for example, by hitting the Faraday cup. These losses affect only the $O^+ + D$ dissociation channel, and they are corrected using the expected symmetries as explained in the Supporting Information, specifically, the cylindrical symmetry about the linear polarization, i.e., a uniform $N(\phi)$, and the reflection symmetry about $\theta = 90°$ where θ is the angle between the dissociation velocity and the polarization.[16,19,21,24−27]

It is important to note that the laser interaction with the molecular ions takes place inside a spectrometer which accelerates the ions away from the detector and thus enables identification of the charged fragments by their time-of-flight (TOF). Additional details of this experimental method are reported in refs 16, 19, 23, 28, and 29.

The KER spectra of $D^+ + O$ and $O^+ + D$ products, measured in coincidence, are shown in Figure 3. The main KER peak is

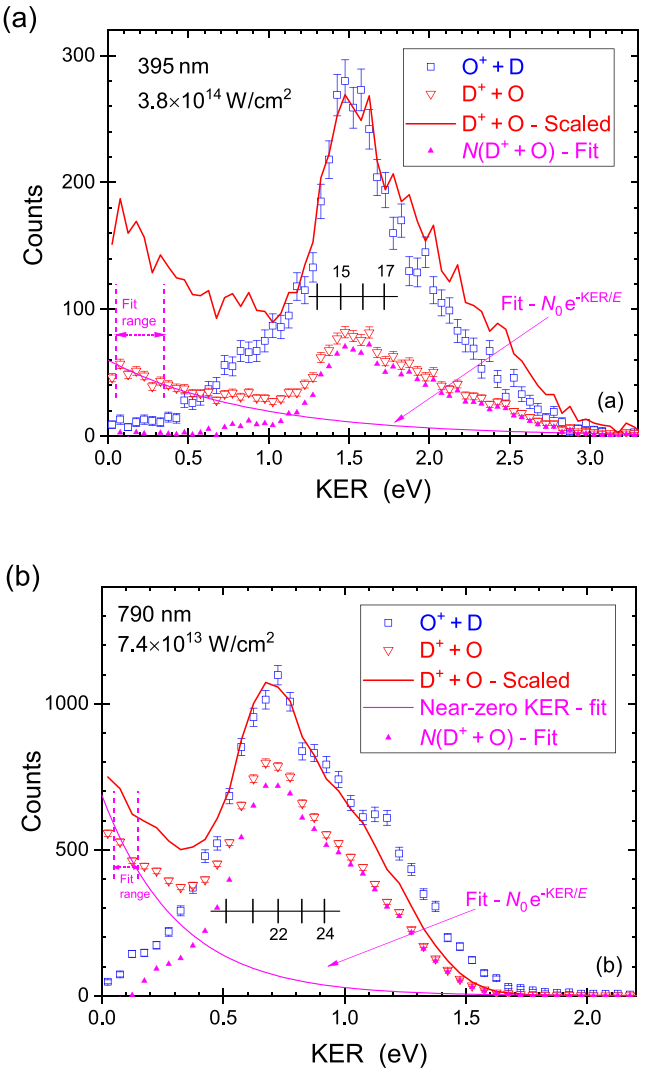

Figure 3. Measured KER distribution of $D^+ + O$ (red) and $O^+ + D$ (blue) channels following photodissociation of OD^+ by (a) ∼ 40 fs, 395 nm, and 3.8×10^{14} W/cm^2 pulses and (b) ∼ 28 fs, 790 nm, and 7.4×10^{13} W/cm^2 pulses (error bars are statistical). The solid red line represents the $D^+ + O$ data scaled to match the $O^+ + D$ peak indicating the similarity of the distributions. The expected KER for photodissociation of a few ($X\,^3\Sigma^-$) vibrational states are marked. The near-zero KER feature is fitted by $N_0e^{-KER/E}$ (solid magenta line) and then subtracted from the measured $N(D^+ + O)$ (solid magenta triangles) (see text).

centered around 1.5 and 0.7 eV for 395 and 790 nm photons, respectively. These KER values are expected for photodissociation driven by excitation to the B $^3\Sigma^-$ state by absorption of a single photon, as shown in Figure 1. The energy shift of the peak centroid with changing photon energy is also consistent with the interpretation above. This structureless peak (within the experimental accuracy) dominates the KER spectrum and is central to our work here. However, the $D^+ + O$ channel exhibits an additional KER feature that is peaked near zero.

https://doi.org/10.1021/acs.jpclett.4c00649
J. Phys. Chem. Lett. 2024, 15, 6859−6865

The high-energy tail of the near-zero KER feature overlaps the main KER peak, and therefore to accomplish our goal discussed below, it should be subtracted. To that end, we note that this tail can be described well by an exponential function of the form $N_0e^{-KER/E}$, where E and N_0 are fit parameters. We fitted this function over the specific KER range shown in Figure 3, where the main KER peak contribution is small. The fitted "KER tail" is then subtracted from the $N(D^+ + O)$ distribution resulting in the $N'(D^+ + O)$ distribution, shown as solid magenta triangles in Figure 3. This $N'(D^+ + O)$ is given explicitly by

$$N'(D^+ + O) = N(D^+ + O) - N_0e^{-KER/E} \quad (1)$$

and is associated with the photodissociation mechanism described above.

Before we explore further the single-photon dissociation process responsible for the main KER peak, it is worth examining briefly the underlying mechanism responsible for the near-zero KER feature, which is more complex than the former mechanism. The near-zero KER feature—appearing only in the $D^+ + O$ channel (as shown in Figure 3)—increases more rapidly with the peak intensity of the laser pulse than the main KER peak, suggesting possible multiphoton processes. The angular distribution of the near-zero KER feature (at 790 nm) is predominantly aligned along (i.e., parallel to) the laser polarization (as shown in the Supporting Information), and this "eliminates" most transitions between the states shown in Figure 1 as candidates because parallel transitions are expected between states with the same angular momentum quantum number[30,31] (and, of course, the same spin multiplicity). For example, a two-photon $X\ ^3\Sigma^- \rightarrow A\ ^3\Pi \rightarrow X\ ^3\Sigma^-$ pathway is expected to be perpendicular to the laser polarization and therefore not important here. The low-lying states of OD^+ suggest that vibrational excitation driven by the permanent dipole, which is seldom observed experimentally,[32] is the underlying mechanism leading to the near-zero KER feature. For instance, vibrational transitions from the bound $X\ ^3\Sigma^-$ to its vibrational continuum above the $D^+ + O(^3P)$ limit, or from the metastable $a\ ^1\Delta$ or $b\ ^1\Sigma^+$ states to their vibrational continuum above the $D^+ + O(^1D)$ dissociation limit, are all expected to favor breakup along the laser polarization. In contrast, the angular distribution measured at 395 nm is uniform, suggesting a different dissociation pathway at play. The most likely dissociation paths in this case involve vibrational excitation of the metastable $a\ ^1\Delta$ or $b\ ^1\Sigma^+$ to vibrational states above the $D^+ + O(^3P)$ dissociation limit, as those are known to predissociate on the subnanosecond time scale.[13,33,34] Given that their lifetimes are much longer than the rotational period, a uniform angular distribution is expected. The specifics of this interesting mechanism require further investigation and that goes beyond the scope of this work.

Now, returning to the main KER peaks, we note that they are similar for both dissociation channels, namely $D^+ + O$ and $O^+ + D$, as shown by the scaled distribution in Figure 3, except for the overall yield that is higher for the $O^+ + D$ channel, which is the dissociation limit of the excited $B\ ^3\Sigma^-$ state. This similarity of the KER distributions suggests that the dissociation to $D^+ + O$ is initiated by photoexcitation to the $B\ ^3\Sigma^-$ state, i.e., the same excitation leading to $O^+ + D$ dissociation, but in this case the excitation is followed by a unimolecular charge-transfer transition to an OD^+ state with a $D^+ + O$ dissociation limit, for example, the $X\ ^3\Sigma^-$ and $A\ ^3\Pi$ states shown in Figure 1. To verify this interpretation, determine which of these states is the main path to $D^+ + O$ dissociation following the $X\ ^3\Sigma^- \rightarrow B\ ^3\Sigma^-$ excitation, and establish the mechanism responsible for the charge transfer transitions, we turn to a theoretical treatment of this process.

While the $A\ ^3\Pi$ and $X\ ^3\Sigma^-$ states can both couple to the $B\ ^3\Sigma^-$ state, the electronic orbital angular momentum coupling between the A and B states is facilitated by a matrix element describing the electronic orbital angular momentum coupling, as laid out by Wolniewicz et al.[35] This matrix element falls off as $1/R^2$, but since the angular coupling derives from the nuclear kinetic energy, it enters the Hamiltonian with a factor of 1 over the reduced mass ($1/\mu_{OD} = 1/3264$ au) and is, hence, very small. Nonadiabatic coupling between the $B\ ^3\Sigma^-$ and $X\ ^3\Sigma^-$ states is significant after the O−D bond stretches somewhat and enables charge-transfer transitions that move population from the excited $B\ ^3\Sigma^-$ state to the $X\ ^3\Sigma^-$ state. Once the dissociation proceeds on the $X\ ^3\Sigma^-$ state, it leads to the $D^+ + O(^3P)$ limit.

To quantify the dissociation mechanism described above, we carried out a coupled two-state time-dependent wavepacket treatment of the OD^+ dissociation dynamics. The initial wavepacket is defined as the product of a specific vibrational wave function of the $X\ ^3\Sigma^-$ ground state of OD^+ and the $X \rightarrow B$ transition dipole moment, $D(R)$, promoted onto the dissociative $B\ ^3\Sigma^-$ potential.[36] The initial wavepacket is then propagated on the two states, coupled by the nonadiabatic radial derivative operator, and the cross sections can be evaluated from the Fourier transform of the asymptotic flux.[37] Note that although the cross sections are obtained as a continuous function of KER, there is only one physical value at fixed photon energy for each initial vibrational state that is consistent with energy conservation (see Figure 1).

Figure 4 shows our computed potential parameters for the $\nu = 22$ level of the X-state. The upper panel shows the $X \rightarrow B$ dipole moment, $D(R)$, the $\nu = 22$ vibrational wave function, Ψ_X, and the initial wavepacket Ψ_B, which is the product of Ψ_X and $D(R)$. The lower panel of Figure 4 shows the coefficient of the nonadiabatic radial derivative operator. We found that the computed cross sections for 395 and 790 nm photons peak at $\nu = 16$ and $\nu = 22$, respectively, consistent with the measured yields shown in Figure 3, but unlike the measured values, do not form a smooth distribution about the peak values. This finding is due not only to the discrete nature of the computed cross sections, which vary rapidly for high vibrational quantum number, but more significantly to the neglect of rotational effects in the calculations, which were carried out for $J = 0$ only, since we could not determine the distribution of rotational levels in the OD^+ beam.

The charge-transfer transition probability is determined to be the branching ratio of the measured $D^+ + O$ dissociation channel at each KER value, given explicitly by

$$BR(KER) = \frac{N'_{D^+ + O}(KER)}{N'_{D^+ + O}(KER) + N_{O^+ + D}(KER)} \quad (2)$$

where $N'_{D^+ + O}(KER)$ and $N_{D^+ + O}(KER)$ are the number of counts in the $D^+ + O$ and $O^+ + D$ dissociation channels with a specific KER value, i.e., the number of counts in the KER distributions shown in Figure 3. We assume, in eq 2, that all

https://doi.org/10.1021/acs.jpclett.4c00649
J. Phys. Chem. Lett. 2024, 15, 6859−6865

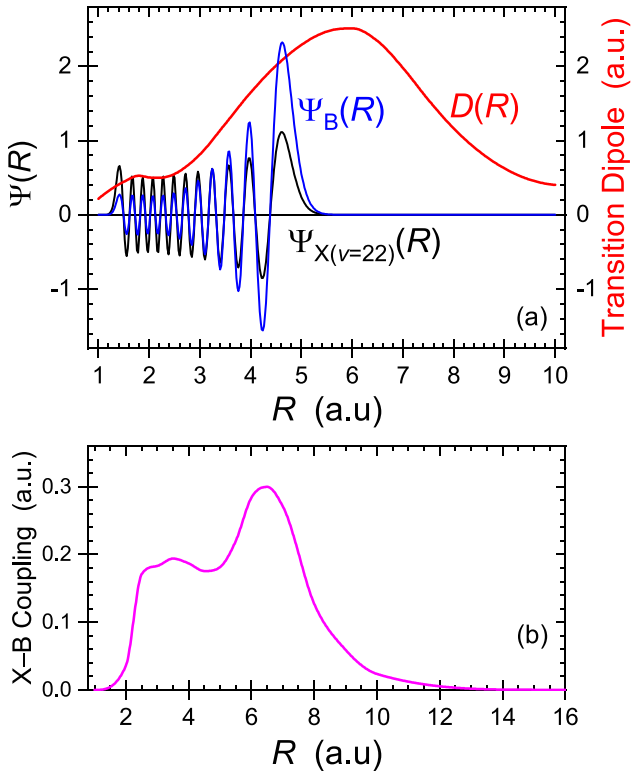

Figure 4. (a) A vibrational wave function, $\Psi_{v=22}(R)$, on the OD^+ electronic ground state (black), photoexcited by the transition dipole moment (red) to the excited B $^3\Sigma^-$ state, yielding a wave function, $\Psi_B(R)$ (blue), which is then propagated on the excited state. (b) The X–B radial coupling driving unimolecular charge-transfer transitions from the B $^3\Sigma^-$ state to the X $^3\Sigma^-$ state, which is associated with the $D^+ + O(^3P)$ limit.

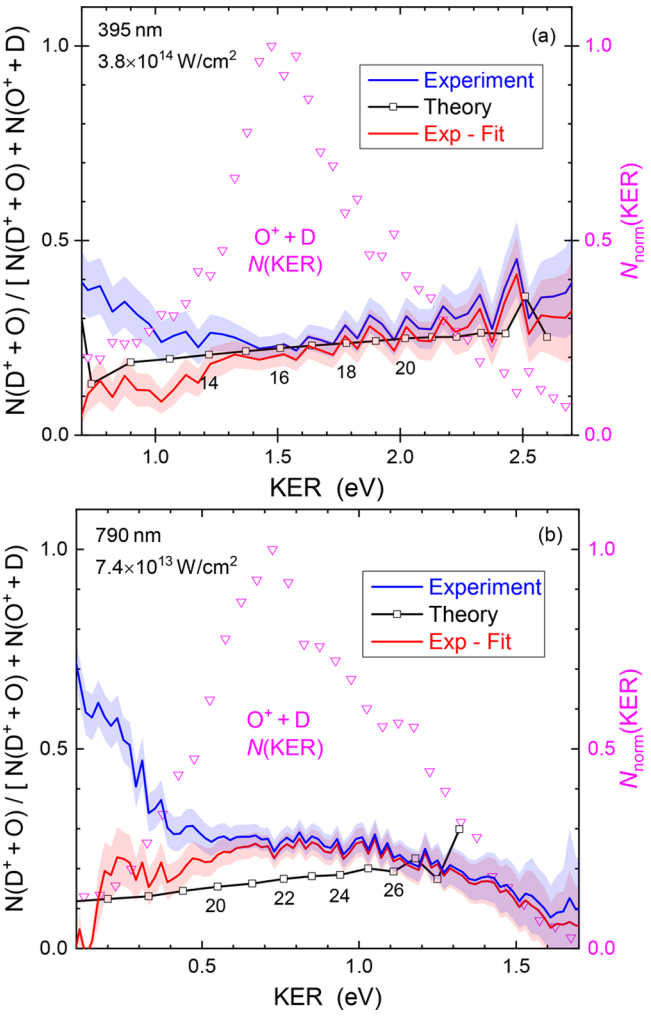

Figure 5. Measured (solid blue and red lines) and calculated (black squares and lines) branching ratio of OD^+ dissociation to $D^+ + O$ (relative to the sum of both channels) as a function of KER for (a) 395 nm and (b) 790 nm. The red lines include subtraction of the near-zero KER feature while the blue lines do not (see text). Errors are at the one sigma level (shaded band), and the KER distribution (magenta symbols) indicates the KER range for which the branching ratio, i.e., the B $^3\Sigma^-$ to X $^3\Sigma^-$ transition probability, is determined well experimentally. Note that the calculated branching ratios are terminated where the yields are too small to calculate a meaningful branching ratio.

fragments have the same detection efficiency, so those efficiencies cancel out. This is accomplished by tuning the voltage gain of both MCP detectors well within the saturation regime[38] and using a beam energy for which the impact energy of all fragments is sufficient to reach the maximum detection efficiency[39−41] (see the Supporting Information for further details). Then, to compare with theory, the N values in eq 2 are replaced with the computed ν-dependent cross sections.

Recall that $N'_{D^+ + O}(\mathrm{KER})$ was corrected, by subtracting contributions from the near-zero KER feature using eq 1, and therefore this number represents dissociation into $D^+ + O$ following a X $^3\Sigma^-$ to B $^3\Sigma^-$ excitation by absorption of a single photon. This is a necessary condition that allows us to associate the measured $D^+ + O$ branching ratio given in eq 2 with the unimolecular B $^3\Sigma^-$ to X $^3\Sigma^-$ charge transfer transition probability. In Figure 5a we show a direct comparison between the measured branching ratio evaluated with and without subtraction of the near-zero KER tail, which shows that this correction is negligible above a KER of about 1.1 eV because the energy spacing between the two KER features is large enough at 395 nm. In contrast, this spacing is much smaller for 790 nm, and therefore this correction is more critical.

The branching ratios measured with 790 and 395 nm are 0.174 and 0.223, respectively, at the center of each KER peak, and they vary slowly with KER, as shown in Figure 5, where they are compared to the results of our calculations of the B–X transition probability, i.e., the charge transfer probability as a function of energy above the dissociation limit. Note that the KER is equivalent to the energy above the $D^+ + O(^3P)$ dissociation limit, and the extremely small (~20 meV) energy difference to the $O^+(^4S) + D$ dissociation limit can be neglected. Evidently, there is nice agreement between theory and experiment, especially over the range where this photodissociation process is likely, i.e., N(KER) is significant. It is noticeable that the agreement between the 790 nm data and theory is slightly inferior to the 395 nm data (see direct comparison between the two measurements in the Supporting Information), as a result of the subtraction of the low-KER feature (due to the limited fitting range (see Figure 3).

In summary, we measured the photodissociation of OD^+ to $D^+ + O$ and $O^+ + D$ employing a coincidence momentum imaging technique that was enabled by the use of an upgraded two-detector setup. In this experiment, we have identified the

https://doi.org/10.1021/acs.jpclett.4c00649
J. Phys. Chem. Lett. 2024, 15, 6859−6865

main photodissociation path of OD^+ into either $D^+ + O$ or $O^+ + D$, which in both cases is initiated by a X $^3\Sigma^-$ to B $^3\Sigma^-$ dipole transition. This photoexcitation dominates the KER spectrum measured with either 790 or 395 nm pulses. The dissociation on the excited B $^3\Sigma^-$ state leads directly to the $O^+(^4S) + D$ dissociation limit. In contrast, dissociation to the nearly degenerate $D^+ + O(^3P)$ limit requires a unimolecular charge transfer transition, which according to our theoretical treatment involves a B $^3\Sigma^- \rightarrow$ X $^3\Sigma^-$ transition driven by radial coupling of the stretched O−D bond. The calculated probability for this transition is in good agreement with the charge transfer probability derived from the measurement, specifically the $D^+ + O$ branching ratio as a function of KER.

Finally, this transition probability is the amplitude square (amp = $\sqrt{BR}$) for transitions between the X $^3\Sigma^-$ and B $^3\Sigma^-$ states during $H^+ + O \rightarrow O^+ + H$ charge-exchange reactions, which are a key step in OH production in interstellar clouds. Therefore, the branching ratios reported here may guide theoretical treatment of these collisions at very low energy spanned by our measured KER.

■ ASSOCIATED CONTENT

Supporting Information

The Supporting Information is available free of charge at https://pubs.acs.org/doi/10.1021/acs.jpclett.4c00649.

(1) Experimental details (Figure S1: schematic view of the voltage along the spectrometer); (2) data analysis (Figure S2: OD^+ coincidence time-of-flight spectra; Figure S3: position distribution of the OD^+ fragments; Figure S4: $N(P_r,\phi)$ distributions of OD^+ dissociation channels); (3) angular distributions (Figure S5: N(KER, cos θ) distributions for $D^+ + O$ dissociation channel; Figure S6: similar distribution for the $O^+ + D$ channel); (4) calculated KER distributions (Figure S7: comparison of the calculated and measured KER distributions); (5) detection efficiency considerations (Figure S8: qualitative detection efficiency); (6) direct comparison of branching ratios (Figure S9: comparison of 790 and 395 nm measurements) (PDF)

■ AUTHOR INFORMATION

Corresponding Author

I. Ben-Itzhak − *J. R. Macdonald Laboratory, Department of Physics, Kansas State University, Manhattan, Kansas 66506, United States;* orcid.org/0000-0002-6214-3520; Email: ibi@phys.ksu.edu

Authors

Chandan Bagdia − *J. R. Macdonald Laboratory, Department of Physics, Kansas State University, Manhattan, Kansas 66506, United States*

T. Severt − *J. R. Macdonald Laboratory, Department of Physics, Kansas State University, Manhattan, Kansas 66506, United States*

Naoki Iwamoto − *J. R. Macdonald Laboratory, Department of Physics, Kansas State University, Manhattan, Kansas 66506, United States*

Anjali Filinovich − *J. R. Macdonald Laboratory, Department of Physics, Kansas State University, Manhattan, Kansas 66506, United States*

T. N. Rescigno − *Chemical Sciences Division, Lawrence Berkeley National Laboratory, Berkeley, California 94720, United States*

A. E. Orel − *Chemical Engineering, University of California, Davis, Davis, California 95616, United States*

K. D. Carnes − *J. R. Macdonald Laboratory, Department of Physics, Kansas State University, Manhattan, Kansas 66506, United States*

Complete contact information is available at: https://pubs.acs.org/10.1021/acs.jpclett.4c00649

Notes

The authors declare no competing financial interest.

■ ACKNOWLEDGMENTS

We thank C.W. Fehrenbach for assistance with the PULSAR laser. This work is supported by the Chemical Sciences, Geosciences, and Biosciences Division, Office of Basic Energy Sciences, Office of Science, U.S. Department of Energy, under Award # DE-FG02-86ER13491. Work at LBNL was supported by the same funding agency under Award No. DE-AC02-05CH11231. A.F. acknowledges NSF Award #2244539 for support of the Kansas State University REU program during the summer 2023.

■ REFERENCES

(1) Helm, H.; Cosby, P. C.; Huestis, D. L. Photofragment spectroscopy of shape resonances in OH^+. *Phys. Rev. A* **1984**, *30*, 851−857.

(2) Black, J. H.; Dalgarno, A. Models of interstellar clouds. I. The Zeta Ophiuchi cloud. *Astrophys. J. Supplement Series* **1977**, *34*, 405−423.

(3) Hechtfischer, U.; Levin, J.; Lange, M.; Knoll, L.; Schwalm, D.; Wester, R.; Wolf, A.; Zajfman, D. Near-threshold photodissociation of cool OH^+ to $O + H^+$ and $O^+ + H$. *J. Chem. Phys.* **2019**, *151*, 044303.

(4) Rodgers, D. J.; Sarre, P. J. High-resolution laser photofragment spectroscopy of the c $^1\Pi$ − b $^1\Sigma^+$ system of OH^+. *Chem. Phys. Lett.* **1988**, *143*, 235−239.

(5) Rodgers, D. J.; Batey, A. D.; Sarre, P. J. High-resolution laser spectroscopy and photodissociation dynamics of OH^+. *Mol. Phys.* **2007**, *105*, 849−860.

(6) Levick, A. P.; Masters, T. E.; Rodgers, D. J.; Sarre, P. J.; Zhu, Q.-S. Symmetry-dependent branching between O^++H and O+H^+ dissociation channels in the photofragmentation of OH^+. *Phys. Rev. Lett.* **1989**, *63*, 2216−2219.

(7) Yarkony, D. R. Spin-forbidden predissociation of the rovibronic levels of OH^+(c $^1\Pi$). *J. Phys. Chem.* **1993**, *97*, 111−119.

(8) Spirko, J. A.; Zirbel, J. J.; Hickman, A. P. Quantum mechanical scattering calculations for charge exchange: O+$H^+ \leftrightarrow O^+$+H. *J. Phys. B: At., Mol. Opt. Phys.* **2003**, *36*, 1645−1662.

(9) Spirko, J. A.; Mallis, J. T.; Hickman, A. P. Calculation of adiabatic and diabatic $^3\Sigma^-$ states of OH^+. *J. Phys. B: At., Mol. Opt. Phys.* **2000**, *33*, 2395−2407.

(10) Wells, E.; Carnes, K. D.; Esry, B. D.; Ben-Itzhak, I. Charge transfer and elastic scattering in very slow H^++D(1s) half collisions. *Phys. Rev. Lett.* **2001**, *86*, 4803−4806.

(11) Wells, E.; Carnes, K. D.; Ben-Itzhak, I. Probing very slow H^+ + D(1s) collisions using the ground-state dissociation of HD^+. *Phys. Rev. A* **2003**, *67*, 032708.

(12) Saxe, P. W.; Lengsfield, B. H., III; Martin, R. L.; Page, M. *MESA (Modern Electronic Structure Applications)*; University of California, 1990.

(13) de Vivie, R.; Marian, C. M.; Peyerimhoff, S. D. Spin-forbidden transitions in the presence of an intersystem crossing: Application to the b $^1\Sigma^+$ state in OH^+. *Chem. Phys.* **1987**, *112*, 349−361. We note

that the labels for the B $^3\Sigma^-$ and $^5\Sigma^-$ states in Figure 2 of this paper seem to be reversed.
(14) Hirst, D. M.; Guest, M. F. An ab initio study of the excited states of OH^+. *Mol. Phys.* **1983**, *49*, 1461−1469.
(15) Saxon, R. P.; Liu, B. Theoretical study of OH^+: Potential curves, transition moments,and photodissociation cross sections. *J. Chem. Phys.* **1986**, *85*, 2099−2104.
(16) Severt, T. Imaging light-induced molecular fragmentation dynamics. Ph.D. thesis, Kansas State University, 2021.
(17) Sidky, E. Y.; Ben-Itzhak, I. Phase-amplitude method for calculating resonance energies and widths for one-dimensional potentials. *Phys. Rev. A* **1999**, *60*, 3586−3592.
(18) Gaire, B.; McKenna, J.; Zohrabi, M.; Carnes, K. D.; Esry, B. D.; Ben-Itzhak, I. Dynamics of D_3^+ slow dissociation induced by intense ultrashort laser pulses. *Phys. Rev. A* **2012**, *85*, 023419.
(19) Gaire, B. Imaging of slow dissociation of the laser induced fragmentation of molecular ions. Ph.D. thesis, Kansas State University, 2011.
(20) McKenna, J.; Sayler, A. M.; Gaire, B.; Johnson, N. G.; Parke, E.; Carnes, K. D.; Esry, B. D.; Ben-Itzhak, I. Intensity dependence in the dissociation branching ratio of ND^+ using intense femtosecond laser pulses. *Phys. Rev. A* **2008**, *77*, 063422.
(21) Graham, L.; et al. Fragmentation of CD^+ induced by intense ultrashort laser pulses. *Phys. Rev. A* **2015**, *91*, 023414.
(22) RoentDek RoentDek Handels GmbH. http://www.roentdek.com.
(23) Sayler, A. M. Measurements of ultrashort intense laser-induced fragmentation of simple molecular ions. Ph.D. thesis, Kansas State University, 2008.
(24) McKenna, J.; Anis, F.; Sayler, A. M.; Gaire, B.; Johnson, N. G.; Parke, E.; Carnes, K. D.; Esry, B. D.; Ben-Itzhak, I. Controlling strong-field fragmentation of H_2^+ by temporal effects with few-cycle laser pulses. *Phys. Rev. A* **2012**, *85*, 023405.
(25) Jochim, B.; Erdwien, R.; Malakar, Y.; Severt, T.; Berry, B.; Feizollah, P.; Rajput, J.; Kaderiya, B.; Pearson, W. L.; Carnes, K. D.; Rudenko, A.; Ben-Itzhak, I. Three-dimensional momentum imaging of dissociation in flight of metastable molecules. *New J. Phys.* **2017**, *19*, 103006.
(26) Severt, T.; Daugaard, D. R.; Townsend, T.; Ziaee, F.; Borne, K.; Bhattacharyya, S.; Carnes, K. D.; Rolles, D.; Rudenko, A.; Wells, E.; Ben-Itzhak, I. Two-body dissociation of formic acid following double ionization by ultrafast laser pulses. *Phys. Rev. A* **2022**, *105*, 053112.
(27) Jochim, B. Dissociation dynamics of molecular ions in ultrafast, intense laser fields: from diatomic to polyatomic molecules. Ph.D. thesis, Kansas State University, 2019.
(28) Ben-Itzhak, I.; Wang, P. Q.; Xia, J. F.; Sayler, A. M.; Smith, M. A.; Carnes, K. D.; Esry, B. D. Dissociation and ionization of H_2^+ by ultrashort intense laser pulses probed by coincidence 3D momentum imaging. *Phys. Rev. Lett.* **2005**, *95*, 073002.
(29) Wang, P. Q.; Sayler, A. M.; Carnes, K. D.; Xia, J. F.; Smith, M. A.; Esry, B. D.; Ben-Itzhak, I. Dissociation of H_2^+ in intense femtosecond laser fields studied by coincidence three-dimensional momentum imaging. *Phys. Rev. A: At., Mol., Opt. Phys.* **2006**, *74*, 043411.
(30) Hishikawa, A.; Liu, S.; Iwasaki, A.; Yamanouchi, K. Light-induced multiple electronic-state coupling of O_2^+ in intense laser fields. *J. Chem. Phys.* **2001**, *114*, 9856−9862.
(31) Sayler, A. M.; Wang, P. Q.; Carnes, K. D.; Esry, B. D.; Ben-Itzhak, I. Determining laser-induced dissociation pathways of multielectron diatomic molecules: Application to the dissociation of O_2^+ by high-intensity ultrashort pulses. *Phys. Rev. A* **2007**, *75*, 063420.
(32) Jochim, B.; Zohrabi, M.; Gaire, B.; Anis, F.; Uhlíková, T.; Carnes, K. D.; Wells, E.; Esry, B. D.; Ben-Itzhak, I. Direct evidence of the dominant role of multiphoton permanent-dipole transitions in strong-field dissociation of NO^{2+}. *Phys. Rev. A* **2022**, *105*, 043101.
(33) Gervais, B.; Giglio, E.; Adoui, L.; Cassimi, A.; Duflot, D.; Galassi, M. E. The H_2O^{2+} potential energy surfaces dissociating into H^+/OH^+: Theoretical analysis of the isotopic effect. *J. Chem. Phys.* **2009**, *131*, 024302.
(34) Severt, T.; et al. Step-by-step state-selective tracking of fragmentation dynamics of water dications by momentum imaging. *Nat. Commun.* **2022**, *13*, 5146.
(35) Wolniewicz, L.; Orlikowski, T.; Staszewska, G. $^1\Sigma_u$ and $^1\Pi_u$ states of the hydrogen molecule: Nonadiabatic couplings and vibrational levels. *J. Mol. Spectrosc.* **2006**, *238*, 118−126.
(36) Heller, E. Quantum corrections to classical photodissociation models. *J. Chem. Phys.* **1978**, *68*, 2066−2075.
(37) Jaeckle, A.; Meyer, H.-D. Time-dependent calculation of reactive flux employing complex absorbing potentials: General aspects and application within the multiconfiguration time-dependent Hartree wave approach. *J. Chem. Phys.* **1996**, *105*, 6778−6786.
(38) Straub, H. C.; Mangan, M. A.; Lindsay, B. G.; Smith, K. A.; Stebbings, R. F. Absolute detection efficiency of a microchannel plate detector for kilo-electron volt energy ions. *Rev. Sci. Instrum.* **1999**, *70*, 4238−4240.
(39) Gao, R. S.; Gibner, P. S.; Newman, J. H.; Smith, K. A.; Stebbings, R. F. Absolute and angular efficiencies of a microchannel-plate position-sensitive detector. *Rev. Sci. Instrum.* **1984**, *55*, 1756−1759.
(40) Brehm, B.; Grosser, J.; Ruscheinski, T.; Zimmer, M. Absolute detection efficiencies of a microchannel plate detector for ions. *Meas. Sci. Technol.* **1995**, *6*, 953−958.
(41) Takahashi, N.; Hosokawa, S.; Saito, M.; Haruyama, Y. Measurement of absolute detection efficiencies of a microchannel plate using the charge transfer reaction. *Phys. Scr.* **2011**, *T144*, 014057.

https://doi.org/10.1021/acs.jpclett.4c00649
J. Phys. Chem. Lett. 2024, 15, 6859−6865